Gap engineering and wave function symmetry in C and BN armchair nanoribbons

Elisa Serrano Richaud,[1] Sylvain Latil,[2] Hakim Amara,[1,3] and Lorenzo Sponza[1,4]
[1]*Université Paris-Saclay, ONERA, CNRS, Laboratoire d'Étude des Microstructures (LEM), 92322 Châtillon, France*
[2]*Université Paris-Saclay, CEA, CNRS, SPEC, 91191 Gif-sur-Yvette, France*
[3]*Université Paris Cité, Laboratoire Matériaux et Phénomènes Quantiques (MPQ), CNRS-UMR7162, 75013 Paris, France*
[4]*European Theoretical Spectroscopy Facility (ETSF), B-4000 Sart Tilman, Liège, Belgium*

(Received 8 March 2023; revised 22 March 2024; accepted 15 May 2024; published 20 June 2024)

There are many ways of engineering the band gap of nanoribbons, including application of stress, electric field, and functionalization of the edges. In this paper, we investigate separately the effects of these methods on armchair graphene and boron nitride nanoribbons. By means of density functional theory calculations, we show that, despite their similar structures, the two materials respond in opposite ways to these stimuli. By treating them as perturbations of a heteroatomic ladder model based on the tight-binding formalism, we connect the two behaviors to the different symmetries of the top valence and bottom conduction wave functions. These results indicate that opposite and complementary strategies are preferable to engineer the gap width of armchair graphene and boron nitride nanoribbons.

DOI: 10.1103/PhysRevB.109.235425

I. INTRODUCTION

In the last decades, graphene (Gr) and hexagonal boron nitride (BN) monolayers have attracted a great deal of interest because of their remarkable transport and optical properties [1–5]. A much explored way to modulate them is by a further reduction of their size like in 2D quantum dots, nanoribbons, or nanotubes. Confinement comes with novel size-dependent features dominated by geometrical parameters and by the characteristics of the edge itself. This is why nanoribbons are often classified according to their edge shape, which can be zigzag, armchair, or structured in a more complex manner [6]. As a matter of fact, the edge characteristics are crucial for the performances of nanoribbon-based devices such as transistors, interconnects, and logical devices [7–12], photovoltaic applications [12,13], or chemical sensing [12,14]. Gr zigzag nanoribbons have well-localized edge states which confer them antiferromagnetic properties [6,15–20], while BN zigzag nanoribbons have an indirect gap and display an intrinsic dipole moment [17,21–28]. At variance, both Gr [6,11,16–20,23,29–36] and BN [17,22–28] armchair nanoribbons (AGNR and ABNNR), have no magnetic states and display a direct band gap whose energy depends on the width of the ribbon. To take full advantage of this richness of properties, several strategies have been explored to engineer the band gap including, among others [13,16,21,37,38], application of external electromagnetic fields [17,18,22,23,25,34], of stress [27,31], or edge functionalization by chemical passivation [8,11,24,28–33,35,36].

In this paper, we systematically investigate the response of Gr and BN armchair nanoribbons to these different strategies. The size of each ribbon is quantified by the width N_a designating the number of longitudinally aligned C–C or B–N dimers as sketched in Fig. 1. To indicate a specific nanoribbon, we append N_a after the type of material, e.g., AGNR-5 indicates an armchair Gr nanoribbon of width $N_a = 5$. Simulations carried out within density functional theory (DFT) include hydrogens always passivating the edges and all structures are fully relaxed, i.e., both in-plane atomic coordinates and the cell parameter a are optimized. We focus our investigation on the evolution of the gap as a function of N_a upon application of uniaxial stress, biaxial stress, and external electric fields. We also explore the impact of edge functionalization by dividing it into an electrostatic and deformation component. For further details on the parameters of the calculations, see Appendix A.

The paper is divided as follows: In Sec. II A, we discuss the variations of the gap width upon stimuli corresponding to the different gap engineering strategies simulated at the DFT level. Successively (Sec. II B), we extend to the heteroatomic case a tight-binding ladder model [6,18,20] to investigate the response of the two materials. In Sec. III, we discuss in more detail the specific case of H passivation solving the ladder model numerically and comparing it with analytical perturbative formulas. Conclusions are summarized in Sec. IV. Appendixes A and B are about computational details and some useful mathematical relations.

II. BAND-GAP ENGINEERING

A. Opposite and complementary responses

The electronic structure of BN and Gr nanoribbons has been thoroughly studied in the past [6,11,15,16,17,18,19,20–36]. Our DFT band gap of ABNNRs and AGNRs for widths ranging from $N_a = 5$ to $N_a = 19$ are reported in red in the two panels of Fig. 2 and are in good agreement with similar calculations in literature. We recall that, owing to the 1D confinement, the gap width of both materials falls in one of the three families: $N_a = 3m - 1$, $N_a = 3m$ or $N_a = 3m + 1$ (with $m \in \mathbb{N}*$). The ordering of the families is the same in the two materials, with the $N_a = 3m - 1$ branch always lowest in energy. We remark that size effects on thinner ribbons can be quite large: in ABNNRs, the gap variation is roughly ± 0.1 eV with respect to the asymptoptic limit, which happens to be

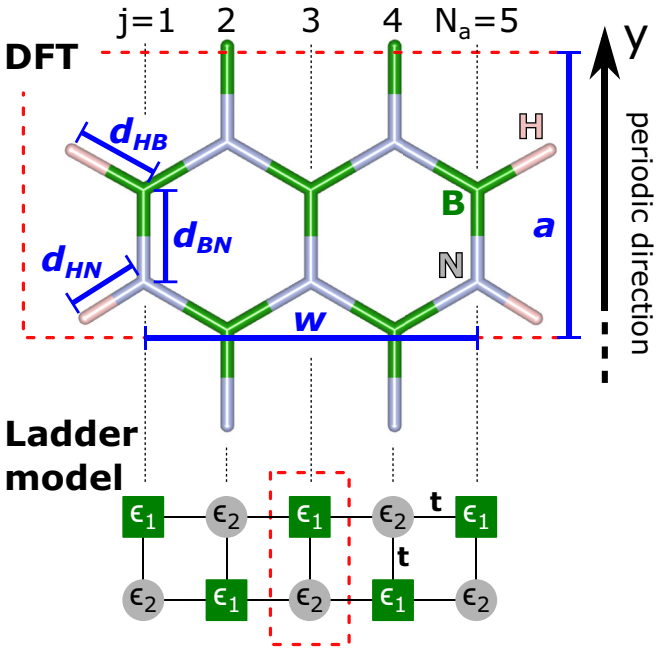

FIG. 1. Top: Structure of the reference ABNNR-5. Vertical dotted lines enumerate the rows. In blue, we highlight the cell parameter a, the width w, and the notable lengths d_{HB}, d_{HN}, and d_{BN}. H, N, and B atoms are placed, respectively, in pink, grey, and green lattice sites. AGNRs are analogously structured with the relevant edge lengths are labeled d_{HC} and d_{CC}. Bottom: The corresponding two-atom ladder model. Sites labeled $\mu = 1$ are drawn with squares and $\mu = 2$ with circles. The color code is the same as in the panel above. The homoatomic ladder model is defined by $\epsilon_1 = \epsilon_2 = 0$.

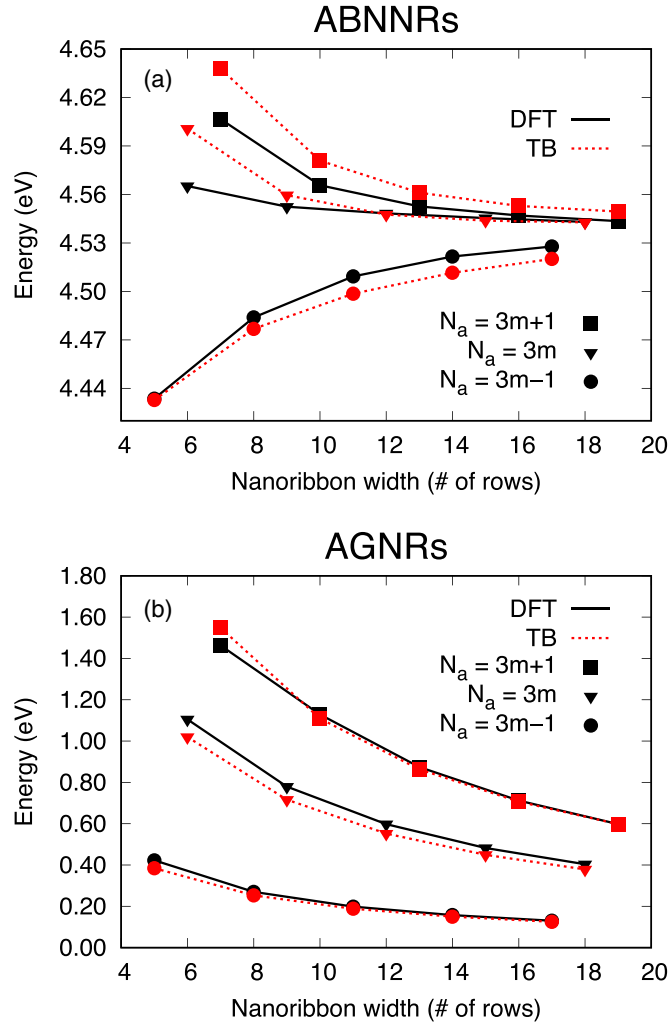

FIG. 2. Gap of ABNNRs (a) and AGNRs (b) as a function of N_a. Different symbols are associated to different families. Black solid line: DFT calculations. Red dashed line: numerical diagonalization of the ladder model parametrized as in Table I.

lower than in the isolated monolayer because of a residual edge contribution [22,24]. In AGNRs, size effects are even stronger, the gap opens up to 1.6 eV at width $N_a = 7$ and ranges between 0.1 and 0.4 in the $N_a = 3m - 1$ family.

We can now proceed with the inclusion of stimuli accounting for different gap engineering strategies. For reasons that will become clearer later, we focus our analysis on the family $N_a = 3m - 1$. In Fig. 3, we report the gap width of ABNNRs (left panels) and AGNRs (right panels) belonging to this family as a function of N_a and under the effect of different stimuli. In all panels, the bulleted black solid lines are the reference band gaps of the fully relaxed calculations (those reported in Fig. 2). Before discussing the details, one result immediately jumps out. The two materials display opposite and complementary responses. When ABNNRs show a violent modification of their gap width, AGNRs show negligible variations and the other way around.

In literature, the effect of a transversal (along x) electric field is predicted to close the gap of ABNNRs already at weak intensity, with stronger variations in wider ribbons [17,22,25]. Instead, in AGNRS, a width-dependent threshold intensity must be passed, below which the gap is constant [17,34]. Our results are reported in Figs. 3(a1) and 3(a2) with green crosses for a field of 0.5 V/nm, corresponding to a very weak field. For the comparison to be meaningful, the field is the same in the two materials. In agreement with literature, DFT predicts a relatively violent gap closing in ABNNRs where it decreases from 4.4 eV to 4.0 eV eV with an approximately linear trend, whereas the gap of AGNRs is basically not affected.

The effect of global stretch is reported in Figs. 3(b1) and 3(b2). In addition to the reference values, we report the band gap of ribbons experiencing the same longitudinal (y), transversal (x), or biaxial stretch. More precisely, a tensile strain of 3% is applied to parameters a, w, or both. This is a very low strain, corresponding to a harmonic elastic regime of deformation [24], but what is most important is that it is the same value for all calculations. At variance from before, here DFT predicts that the gap of ABNNRs undergoes weaker variations than that of AGNRs. Typically, uniaxial variations in ABNNRs are of about 0.1 eV, whereas they reach about 0.3 eV in AGNRs. A comparison with literature is not simple, but, for instance, a stress of 7% produces gap variations of about 0.3 eV in ABNNR-7 [27] and more than the double in AGNR-7 [31]. Interestingly, a biaxial stress has almost no effect on AGNRs, as if its y and x elongation components cancel each other, contrary to what is observed in ABNNRs where the two seem to add in closing the gap by about 0.2 eV.

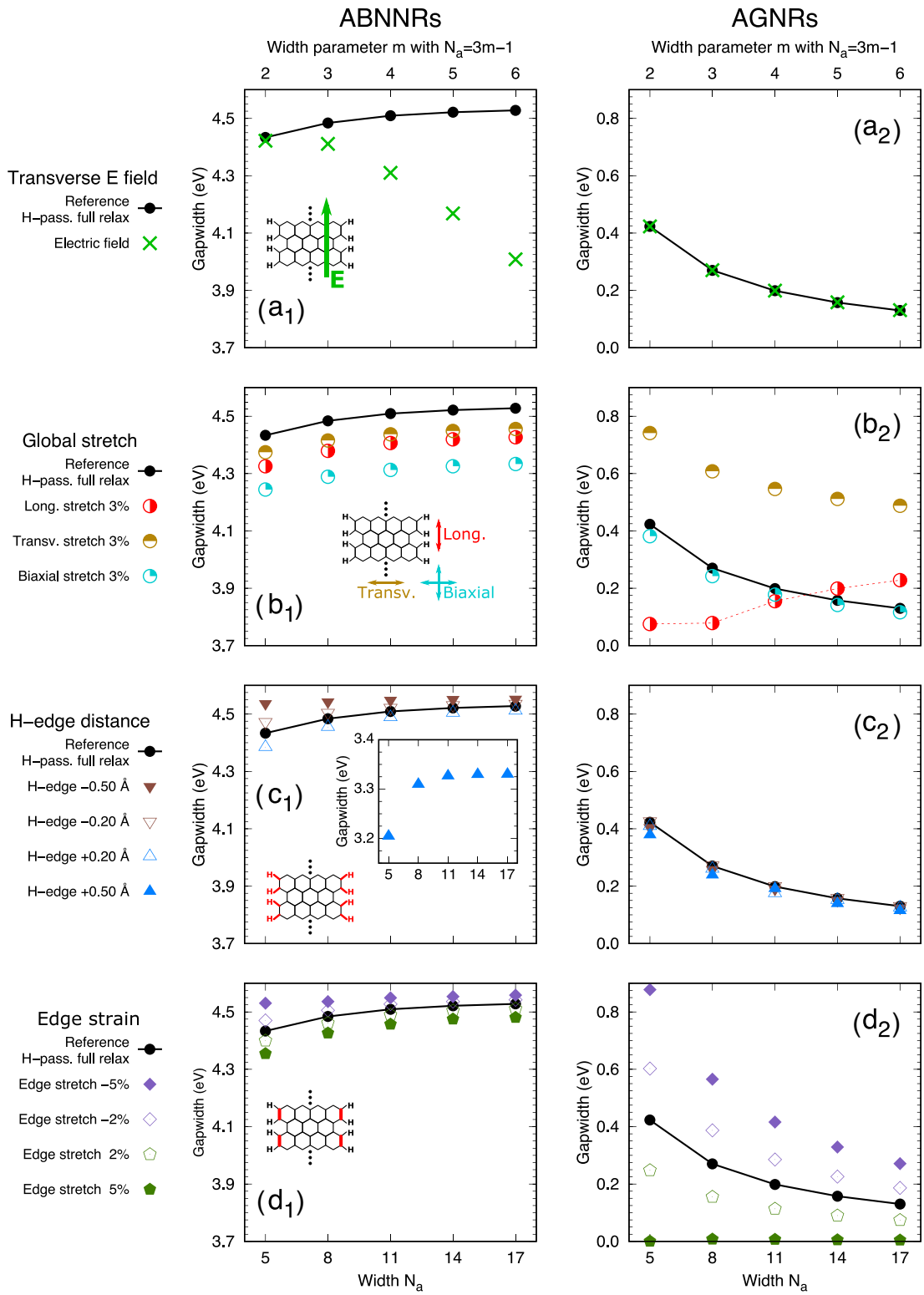

FIG. 3. DFT gap width of ABNNRs (left panels) and AGNRs (right panels) as a function of N_a under the action of stimuli accounting for different gap-engineering strategies suggested by the key title and the structural sketch inside the ABNNR panels. a_1 and a_2: transverse electric field; b_1 and b_2: longitudinal, transversal, and biaxial stretch of 3% (red dashed curve is a guide to the eye); c_1 and c_2: displacement of the passivating H atoms; d_1 and d_2: variation of the bond length at the edges. In all panels, the gap width of the reference H-passivated fully relaxed calculation of Fig. 2 is reported with a bulleted solid black line.

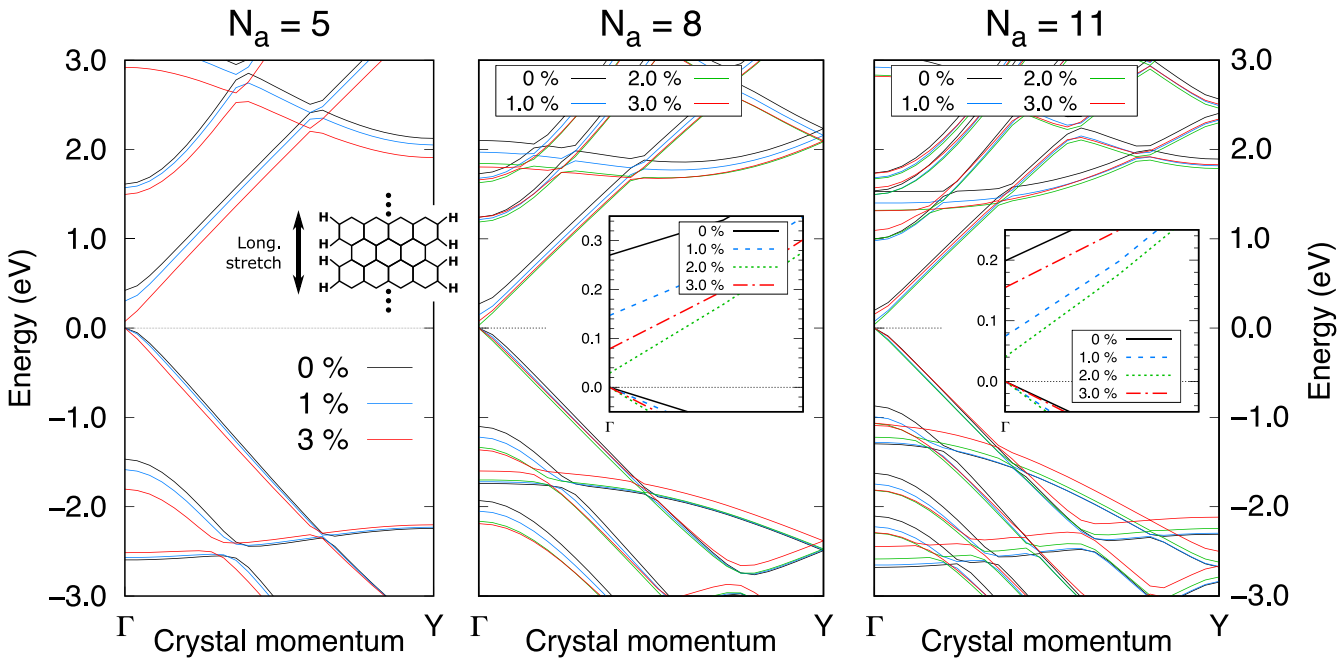

FIG. 4. DFT band structure of AGNRs with $N_a = 5$, 8 and 11 sustaining various longitudinal stresses.

Besides this, a peculiar trend is observed in longitudinally stretched AGNRs, highlighted by a red dashed line. This is related to a sort of *bouncing* of the band gap that closes in small ribbons and opens again in ribbons larger than the characteristic width $N_a \approx 11$. This effect is also visible in the data by Prabhakar and Melnik [31] in the case of AGNR-7. This bouncing behavior can be appreciated more clearly in Fig. 4, where we report the AGNR band structure in the vicinity of the gap for different widths and values of the longitudinal stretch. The higher the stretch, the smaller the critical width.

Edge functionalization is actually a very complex mechanism which may involve global and edge strain, variations of the electrostatic potential felt by all atoms of the ribbon and some charge transfer. Having already addressed global strain, here we concentrate the study on the electrostatic variation in Fig. 4(c) and the edge strain in Fig. 4(d). These separate effects have been studied in the past in the case of AGNRs [20,33]. Here we extend the analysis to ABNNRs and make a quantitative comparison by considering the two contributions separately. In panels c_1 and c_2, we report the gap under variations of d_{HX} of ± 0.2 or ± 0.5 Å ($X = B$, N, or C). Here $+$ signs indicate a displacement away from the edge, $-$signs toward it. Notice that the asymptotic limit of the ABNNR gap width when H atoms are moved 0.50 away from the edges is not the reference gap, but a sizeably smaller one much closer to that of the nonpassivated ribbon [24]. Finally, in panels d_1 and d_2 we report the band gap under expansion (+) and contraction (–) of d_{XY} (with XY = BN or CC) of 2% or 5%. Considered together, these four panels show that edge functionalization efficiently modifies the gap of both materials, though through different mechanisms. While ABNNRs respond mostly to variations of the electrostatic potential, AGNRs are mostly sensitive to the induced strain at the edges, in agreement with literature [20,33]. In both cases, gap variations decrease for increasing width, as expected in the limit of the isolated monolayer (infinite width limit).

Let us now stop here and summarize our results. We have shown that the gap width of ABNNRs is strongly sensitive to variations of the electrostatic environment, indicating the application of electric fields as the most effective way to engineer the gap of ABNNRs. Edge functionalization can be effective on the condition that the electrostatic potential is strongly modified by the passivating species. On the other hand, AGNRs are demonstrated to respond more strongly to mechanically applied uniaxial strain or to the edge strain induced by the functionalization. Such an opposite and complementary response must be rooted in the impact that different stimuli have on the valence band maximum (VBM) and the conduction band minimum (CBM). As a matter of fact, these states have very different localization characteristics in the two materials. While in ABNNRs, the states localize basically on the lattice sites like in the monolayer [39], in AGNRs they are spread along the C–C bonds. As a clear example of this, in Fig. 5 we report the partial density $|\psi(\mathbf{r})|^2$ in Γ of the last occupied and lowest empty states in $N_a = 8$ reference ribbons.

In the next section, we develop a two-atom ladder model to investigate further the consequences of this difference.

B. Two-atom ladder model

Here we employ the tight-binding ladder model which has been initially introduced to study the gap of AGNRs [6,15,16,18,20]. We extend it to the heteroatomic case with the intent of describing both Gr and BN nanoribbons' gap. The resulting heteroatomic ladder model is sketched in the bottom panel of Fig. 1. Electric fields, global strain, and edge functionalization decomposed in its electrostatic and edge-strain components are introduced through first-order perturbation theory via changes of the on-site and hopping parameters of the model, as suggested in Refs. [6,20].

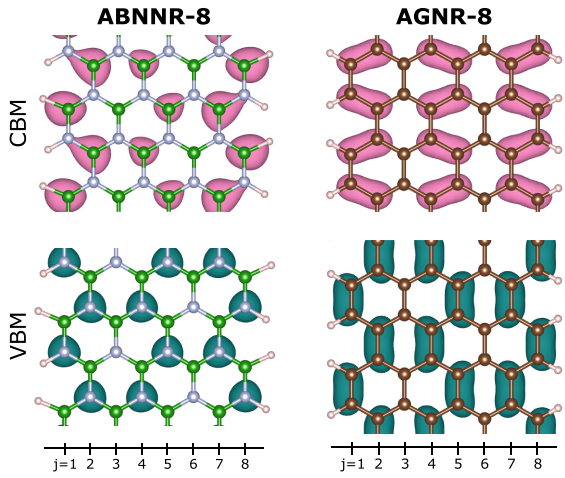

FIG. 5. Reference DFT charge density of the CBM (pink: top panels) and the VBM (dark green: bottom panels) in ABNNR-8 (left panels) and AGNR-8 (right panels). B atoms are placed n green sites, N atoms in grey sites, and C atoms in brown sites. Passivating H atoms are the pink spheres on the edges.

Let us first diagonalize the unperturbed Hamiltonian, which reads

$$H^0 = \sum_{j,\mu} \left(\epsilon_\mu \, |\mu, j\rangle + \sum_{\text{n.n.}} t \, |\mu', j'\rangle \right) \langle \mu, j| \, . \tag{1}$$

The index $j \in [1, N_a]$ labels the row, while $\mu = 1, 2$ indicates both the atomic site and the atomic species in the row (C_1 or C_2 in AGNRs and B or N in ABNNRs). Note that $\mu = 1$ is below $\mu = 2$ in even rows, and vice versa in odd rows. The basis function $\langle \mathbf{r}|\mu, j\rangle$ is the p_z orbital of the atom μ of the jth row. The inner sum is limited to first neighbors and the on-site energies are $\epsilon_1 = -\epsilon_2 = \epsilon$. In ABNNRs, $\epsilon > 0$ to associate N atoms a negative on-site energy and B atoms a positive one [39]. AGNRs are obtained for $\epsilon = 0$.

The discrete spectrum of H^0 is $E^0_{n\pm} = \pm\mathcal{E}_n$, where $n \in [1, ..., N_a]$ and the following definitions are introduced: $\mathcal{E}_n = \sqrt{\epsilon^2 + \tau_n^2}$, $\tau_n = t[1 + 2\cos(\theta_n)]$, and $\theta_n = n\pi/(N_a + 1)$. The $-$ and $+$ signs label occupied and empty states, respectively, which implies that the VBM and the CBM are those that minimize $|\tau_n|$. They are labeled $\tilde{n} = 2m + 1$ in families $N_a = 3m$ and $N_a = 3m + 1$, and $\tilde{n} = 2m$ if $N_a = 3m - 1$. The generic normalized unperturbed eigenstate $|n, \pm\rangle$ reads

$$|n, \pm\rangle = \sqrt{\frac{2}{N_a + 1}} \sum_{j=1}^{N_a} \sin(j\theta_n) \times \left[D_1^{n,\pm} \, |1, j\rangle + D_2^{n,\pm} \, |2, j\rangle \right], \tag{2}$$

with the coefficients

$$D_1^{n\pm} = -\frac{\tau_n}{\sqrt{2\mathcal{E}_n(\mathcal{E}_n \mp \epsilon)}} \quad \text{and} \quad D_2^{n\pm} = \frac{\mp\mathcal{E}_n + \epsilon}{\sqrt{2\mathcal{E}_n(\mathcal{E}_n \mp \epsilon)}}. \tag{3}$$

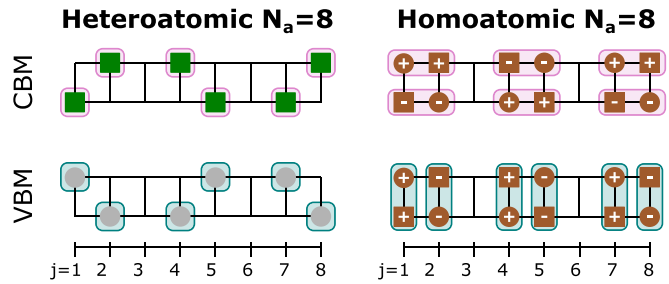

FIG. 6. Representation of the last occupied (VBM) and first unoccupied (CBM) eigenstates of the ladder model. Squares and circles indicate sites with label $\mu = 1$ or $\mu = 2$, respectively. Nodes with no symbol designate sites associated to vanishing total weight by expression (2). In the heteroatomic model, all weights are either $\sqrt{3}/2$ or 0. In the homoatomic one, the $\pm$ symbols are for weights of $\pm\sqrt{3/8}$. Bonding combinations are formed between sites sharing the same sign. Shaded areas highlight the similarity with Fig. 5.

Finally, the unperturbed band gap of the ladder model reads

$$E_g^0 = \begin{cases} 2\epsilon & \text{for } N_a = 3m - 1 \\ 2\mathcal{E}_{2m+1} & \text{for the other values of } N_a. \end{cases} \tag{4}$$

It is worth stopping here to evaluate explicitly the wave functions of the VBM and CBM.

ABNNRs. Since $\tau_{2m} \equiv 0$, in the $N_a = 3m - 1$ family the Hamiltonian of the VBM and CBM is effectively a non-interacting Hamiltonian. The corresponding wave function coefficients read

$$\text{VBM: } D_1^{2m,-} = 0 \quad \text{and} \quad D_2^{2m,-} = 1, \tag{5}$$

$$\text{CBM: } D_1^{2m,+} = 1 \quad \text{and} \quad D_2^{2m,+} = 0, \tag{6}$$

corresponding to pure N states in valence ($\mu = 2$), and pure B states in conduction ($\mu = 1$), as expected in all BN-based materials [39]. These coefficients have to be multiplied by the standing wave envelop $\sin(j\theta_{2m})$. The example for $N_a = 8$ is given in the left panels of Fig. 6 to be compared with the partial charge densities reported in Fig. 5. The ladder model results match extremely well with the first-principles calculations. In the other two families, $|\tau_{2m+1}|$ does not vanish exactly, but is minimized, so the deviation from perfectly pure states is small and actually gets smaller for wider ribbons.

AGNRs. In the homoatomic case, one has to set $\epsilon = 0$ in the Hamiltonian prior to any further manipulation. This condition completely changes the nature of the wave functions, leading to symmetric and antisymmetric combinations of the atomic-centered wave functions. Regardless of the gap family, the coefficients read

$$\text{VBM: } D_1^{\tilde{n},-} = -\frac{\text{sgn}(\tau_{\tilde{n}})}{\sqrt{2}} \quad \text{and} \quad D_2^{\tilde{n},-} = \frac{1}{\sqrt{2}}, \tag{7}$$

$$\text{CBM: } D_1^{\tilde{n},+} = -\frac{\text{sgn}(\tau_{\tilde{n}})}{\sqrt{2}} \quad \text{and} \quad D_2^{\tilde{n},+} = -\frac{1}{\sqrt{2}}. \tag{8}$$

Here $\text{sgn}(x)$ takes value 1 if $x > 0$ and -1 is $x \leqslant 0$. The final wave function at $N_a = 8$, including the envelop prefactors, is reported in the right panels of Fig. 6 and once again the match

with the DFT partial charges of Fig. 5 is excellent. Note that in the $N_a = 3m - 1$ family, it is incorrect to distinguish between VBM and CBM states within the model, because they are actually degenerate [20] at $E^0_{2m,\pm} = 0$. One should rather speak about symmetric (CBM) and antisymmetric (VBM) states, but we will keep the VBM and CBM labeling for convenience.

Now that we solved the unperturbed problem, we can follow the suggestions of Refs. [6,20] and introduce the different band engineering manipulations through a perturbation Hamiltonian δH which includes:

(1) Transverse electric field terms jf_μ with $\mu = 1, 2$. The f_μ perturbative parameters modify the on-site energies of the entire ribbon linearly with the x coordinate of the atomic site, here replaced by the row index $j = 1, ..., N_a$;

(2) Longitudinal (y) and transverse (x) stretch terms $\delta t_\parallel$ and $\delta t_\perp$, respectively, added to all hopping terms depending on their direction.

(3) Edge electrostatic corrections $\delta\epsilon_\mu$ modifying the on-site energies of atoms at the edges (i.e., only on $j = 1$ and $j = N_a$);

(4) Edge stress terms δt_e modifying the hopping between atoms forming the edges, i.e., belonging to rows $j = 1$ and $j = N_a$.

This perturbative Hamiltonian diagonalizes on the basis as

$$\langle \mu, j|\delta H|\mu, i\rangle = [jf_\mu + \delta\epsilon_\mu(\delta_{j,1} + \delta_{j,N_a})]\,\delta_{j,i} \tag{9}$$

for both $\mu = 1$ and $\mu = 2$; and

$$\begin{aligned}\langle 2, j|\delta H|1, i\rangle &= \langle 1, j|\delta H|2, i\rangle \\ &= [\delta t_\parallel + \delta t_e(\delta_{j,1} + \delta_{j,N_a})]\delta_{j,i} \\ &\quad + \delta t_\perp(\delta_{j-1,i} + \delta_{j+1,i}).\end{aligned} \tag{10}$$

The resulting correction to the generic state $\langle n, \pm|\delta H|n, \pm\rangle = \delta F_{n\pm} + \delta S_{n\pm} + \delta C_{n\pm}$ is the sum of three perturbations corresponding to the application of a transverse electric field (δF), the application of uniaxial and/or biaxial stress (δS), and to edge functionalization (δC). After some not so obvious trigonometric manipulation reported in Appendix B, one gets

$$\delta F_{n\pm} = \frac{N_a + 1}{2}\left[\left(D_1^{n\pm}\right)^2 f_1 + \left(D_2^{n\pm}\right)^2 f_2\right], \tag{11}$$

$$\delta S_{n\pm} = 2D_1^{n\pm}D_2^{n\pm}[\delta t_\parallel + 2\cos(\theta_n)\delta t_\perp], \tag{12}$$

and

$$\delta C_{n\pm} = \frac{4\sin^2(\theta_n)}{N_a + 1}\left[2D_1^{n\pm}D_2^{n\pm}\delta t_e + \left(D_1^{n\pm}\right)^2\delta\epsilon_1 + \left(D_2^{n\pm}\right)^2\delta\epsilon_2\right]. \tag{13}$$

The perturbative correction to the band gap is $\delta E_g = \langle\tilde{n}, +|\delta H|\tilde{n}, +\rangle - \langle\tilde{n}, -|\delta H|\tilde{n}, -\rangle$. Note, however, that in the homoatomic $N_a = 3m - 1$ family, since the unperturbed solution is gapless, the absolute value of this expression must be taken. By plugging into this expression the terms (12) and (13), one gets the generic gap correction

$$\begin{aligned}\delta E_g = &\left[\left(D_1^{\tilde{n}+}\right)^2 - \left(D_1^{\tilde{n}-}\right)^2\right]\left[\frac{4\sin^2(\theta_{\tilde{n}})}{N_a + 1}\delta\epsilon_1 + \frac{N_a + 1}{2}f_1\right] + \left[\left(D_2^{\tilde{n}+}\right)^2 - \left(D_2^{\tilde{n}-}\right)^2\right]\left[\frac{4\sin^2(\theta_{\tilde{n}})}{N_a + 1}\delta\epsilon_2 + \frac{N_a + 1}{2}f_2\right] \\ &+ 2\left[D_1^{\tilde{n}+}D_2^{\tilde{n}p+} - D_1^{\tilde{n}-}D_2^{\tilde{n}-}\right]\left[\frac{4\sin^2(\theta_{\tilde{n}})}{N_a + 1}\delta t_e + \delta t_\parallel + 2\cos(\theta_{\tilde{n}})\delta t_\perp\right].\end{aligned} \tag{14}$$

We finally understand why the two materials have different responses to the different stimuli. In fact, if we now insert the wave function coefficients (3) into (14), one finds different band gap corrections for ABNNRs and AGNRs.

ABNNRs. In the heteroatomic solution, for families $N_a = 3m$ and $N_a = 3m + 1$, one gets

$$\begin{aligned}\delta E_g = &\frac{\epsilon}{\mathcal{E}_{2m+1}}\left[\frac{4\sin^2(\theta_{2m+1})}{N_a + 1}(\delta\epsilon_1 - \delta\epsilon_2) + \frac{N_a + 1}{2}(f_1 - f_2)\right] \\ &+ \frac{2\tau_{2m+1}}{\mathcal{E}_{2m+1}}\left[\frac{4\sin^2(\theta_{2m+1})}{N_a + 1}\delta t_e + \delta t_\parallel + 2\cos(\theta_{2m+1})\delta t_\perp\right].\end{aligned} \tag{15}$$

Notice that, since $|\tau_{\tilde{n}}|$ is minimized in the VBM and CBM and it gets closer to 0 as the width increases, the gap correction is dominated by the first term containing only on-site perturbations, i.e., the application of electric fields and the electrostatic component of the edge functionalization. The extreme case of this is encountered in the $N_a = 3m - 1$ family, where $\tau_{\tilde{n}} \equiv 0$ and the wave function coefficients are the pure state combinations reported in expressions (5) and (6). This makes the second term disappear completely and the resulting variation of the gap reads simply

$$\delta E_g = \frac{1}{m}(\delta\epsilon_1 - \delta\epsilon_2) + \frac{3}{2}m(f_1 - f_2). \tag{16}$$

ABNNRs In all families of the homoatomic case, the wave function coefficients are the symmetric and antisymmetric combinations (7) and (8). As a consequence, all the terms modifying on-site energies vanish because of the mutual cancellation of the coefficients $(D_\mu^{\tilde{n}+})^2 - (D_\mu^{\tilde{n}-})^2$ in (14). Instead, the coefficients of the global and edge stress terms add together constructively into $D_1^{\tilde{n}+}D_2^{\tilde{n}+} - D_1^{\tilde{n}-}D_2^{\tilde{n}-} = \mathrm{sgn}(\tau_{\tilde{n}})$. In families $N_a = 3m - 1$ and $N_a = 3m$, this leads to the perturbative gap correction

$$\delta E_g = \mathrm{sgn}(\tau_{\tilde{n}})\left[\frac{8\sin^2(\theta_{2m+1})}{N_a + 1}\delta t_e + 2\delta t_\parallel + 4\cos(\theta_{2m+1})\delta t_\perp\right], \tag{17}$$

whereas in the $N_a = 3m - 1$ family, the final expression reads

$$\delta E_g = 2\left|\frac{1}{m}\delta t_e + \delta t_\parallel - \delta t_\perp\right|. \tag{18}$$

TABLE I. TB parameters in eV for H-passivated nanoribbons. Resulting gaps are reported in Fig. 2.

ABNNR			
$\epsilon_B = -\epsilon_N$	t	$\delta\epsilon$	δt_e
2.285	−2.460	−0.145	−0.190
AGNR			
$\epsilon_{C_1} = \epsilon_{C_2}$	t	$\delta\epsilon$	δt_e
0.0	−2.600	0.0	−0.400

Expressions (16) and (18) indicate how the band gap varies in the family $N_a = 3m - 1$ and can be qualitatively compared with the DFT results of Fig. 3. Concerning the applied field engineering method (panels a_1 and a_2) the model correctly predicts the strong dependence of ABNNRs on the electric field together with its linear dependence on N_a. In the case of applied stress (panels b_1 and b_2), the perturbative formulas predict the right qualitative behavior with the AGNRs, much more sensitive to the ABNNRs (for which there is no variation in the model to be compared with the relatively weak variations predicted by DFT). Also well captured by the model is the opposite sign of $\delta t_\parallel$ and $\delta t_\perp$ in Eq. (18), which indicates two opposite results upon application of longitudinal and perpendicular stress. Even though the gap bouncing discussed earlier cannot be described by our tight-binding (TB) model, the opposite sign predicts the negligible effect of biaxial strain. Coming to the two components of the edge functionalization, the responses predicted by the model are again in very good agreement with the DFT results. According to the formulae, ABNNRs are extremely sensitive to on-site modifications of this gap-engineering method, that is, to the passivation-induced electrostatic variations (panels c_1 and c_2) contrary to AGNRs that are instead more sensitive to the hopping variations, i.e., to the edge strain (panels d_1 and d_2).

The origin of the opposite and complementary response in ABNNRs and AGNRs is now made transparent by the heteroatomic ladder model and is ultimately related to the symmetries of the VBM and CBM in the two materials. In ABNNRs, they are basically pure B or N states, conferring the ribbon a higher sensitivity to on-site variations. In AGNRs, on the contrary, they are basically symmetric and antisymmetric combinations which make the wave functions extend on the bonding. This makes AGNRs much more sensitive to changes of the hopping parameters.

III. LADDER MODEL OF H-PASSIVATED NANORIBBONS

In this section, we provide some additional information on the ladder model when applied to H-passivated ribbons. We retain only the edge-functionalization parameters of δH, namely, $\delta\epsilon_\mu$ and δt_e, and we diagonalize numerically the Hamiltonian $H = H^0 + \delta H$. Successively, we fit by hand the parameters of H against the DFT band gaps reported in Fig. 2. Guided by physical intuitions, we take $\delta\epsilon_1 = \delta\epsilon_2 = \delta\epsilon$ in the case of AGNRs, and $\delta\epsilon_1 = -\delta\epsilon_2 = \delta\epsilon$ in the case of ABNNRs. The resulting parameters and the TB band gap are reported, respectively, in Table I and in Fig. 2 with red dashed lines. Note that we take a nonvanishing value for δt_e in ABNNRs even though its influence should be weak. This is indeed the case in the $N_a = 3m - 1$ family [expression (16)], where large variations of this parameter have minor effects in the gap width, but in the other two families [expression (15)] it is necessary to ensure the right energy ordering.

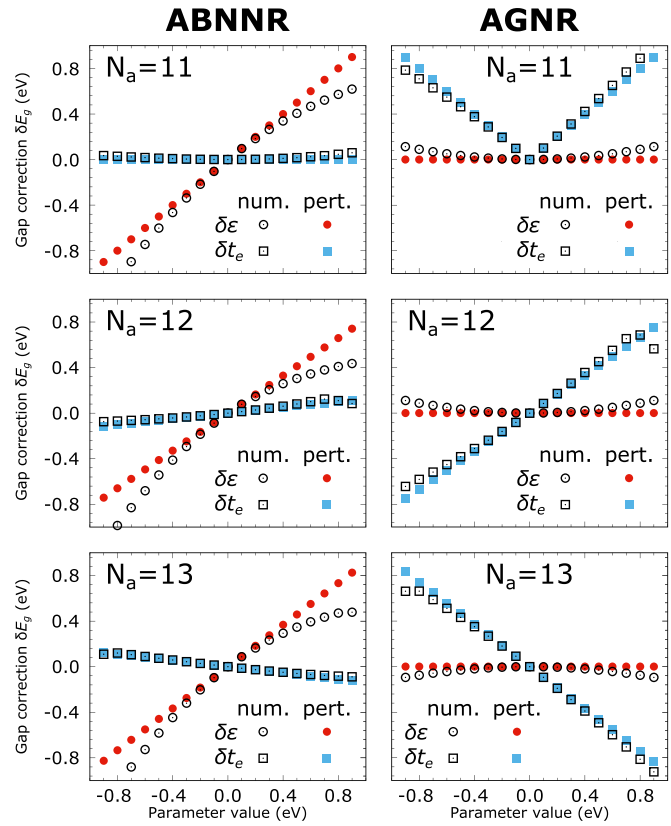

FIG. 7. band gap correction δE_g as a function of δt_e (squares) and $\delta\epsilon$ (circles) in ABNNRs (left panels) and AGNRs (right panels) of width $N_a = 11$, 12 and 13 from top to bottom. Colored symbols: perturbative formulas; Empty symbols: numerical diagonalization.

In addition, we check the range of validity of the perturbative approach by comparing the numerical solution (empty symbols in Fig. 7) with the perturbative formulas (colored symbols) in the range −1 eV, +1 eV in nanoribbons of width N_a=11, 12, and 13, i.e., one representative nanoribbon per family. Globally, the numerical and perturbative results are in very good agreement in the parameter range considered. Deviations of $\delta\epsilon$ are a bit larger than those of δt_e because numerical solutions display a quadratic trend whereas the perturbative formulas are linear in δ_ϵ.

IV. CONCLUSION

We have carried out a comparative study of three gap engineering strategies on armchair BN and Gr nanoribbons, namely, the application of an electric field, of strain and edge functionalization. The latter effect has been divided into two main contributions scrutinized separately: the electrostatic contribution and the deformation of the edges. The study has been conducted by means of DFT calculations and by extending to the heteroatomic case a ladder model which we solved both numerically and perturbatively.

We have shown that the two materials, despite their similarities, respond in opposite and complementary ways to the different modifications they undergo. In particular, while the gap of ABNNRs is much more sensitive to the application of electric field and to the electrostatic component of the edge functionalization, the gap of AGNRs is much strongly modified by the application of stress, being it global or localized on the edges.

The heteroatomic model provides the explanation of this opposite behavior. In fact, the states responsible for the gap formation have very different symmetries in the two materials, being basically pure N or B states in ABNNRs and symmetric or antisymmetric combinations in AGNRs. As a consequence, in ABNNRs the wave functions of the top valence and the bottom conduction are localized on the atomic sites, which makes them much more sensitive to variations of the on-site energies (i.e., electrostatics). On the contrary, in AGNRs the wave functions extend over the bonding between C atoms, causing a much stronger sensitivity to variations of the hopping parameter (i.e., stress).

ACKNOWLEDGMENTS

The authors acknowledge funding from the European Union's Horizon 2020 research and innovation program under Grant Agreement No. 881603 (Graphene Flagship core 3) and from public grants overseen by the French National Research Agency (ANR) under the EXCIPLINT project (Grant No. ANR-21-CE09-0016).

APPENDIX A: COMPUTATIONAL DETAILS

All DFT calculations are carried out within the generalized gradient approximation using the Perdew-Burke-Ernzerhof [40] exchange correlation potential as implemented in the QUANTUM ESPRESSO [41] simulation package. To avoid interactions between consecutive cells, we include 15 Å and 20 Å of empty space in the z and x directions, respectively. In electron density calculations and relaxation runs, the periodic axis is sampled with 20 k-points centered in Γ. This mesh is dense enough to converge total energies in the smallest nanoribbons. We use norm-conserving pseudopotentials [42] and set the kinetic energy cutoff at 80 Ry in both materials.

It is worth stressing that using a large vertical empty space and a high energy cutoff is essential even in the relaxation runs to prevent nearly free-electron states from hanging below the p_z states, hence jeopardizing the gap description. In fact, as already well-known for freestanding layers [43–47] and nanotubes [48–50], in BN nanomaterials there is a competition at the bottom conduction between $2p_z$ and $3s$ states, whose right alignment requires a dedicated convergence study. If sometimes one can overlook this issue in BN layers, because the two competing states create two separate valleys in the Brillouin zone, this is not the case in ABNNRs where both states give rise to a direct gap at Γ.

All reference structures are fully relaxed, allowing optimization of both atomic positions and cell parameter a. Relaxation runs have been performed with the Broyden–Fletcher–Goldfarb–Shanno (BFGS) algorithm with the stopping criterion of all forces being lower than 5×10^{-5} eV/Å. In modified systems (i.e., calculations with applied electric fields, applied global or edge stress, and with H displacements), no additional relaxation has been done.

APPENDIX B: NOTABLE TRIGONOMETRIC IDENTITIES

Some notable trigonometric identities used in the derivation of the tight-binding perturbative corrections:

$$\sin^2(\theta_n) = \sin^2(N_a\theta_n)\,; \tag{B1}$$

$$\sum_{j=1}^{N_a} \sin^2(j\theta_n) = \frac{N_a+1}{2}\,; \tag{B2}$$

$$\sum_{j=1}^{N_a-1} \sin(j\theta_n)\sin\left[(j+1)\theta_n\right] = \frac{N_a+1}{2}\cos(\theta_n)\,; \tag{B3}$$

$$\sum_{j=1}^{N_a} j\sin^2\left(j\theta_n\right) = \left(\frac{N_a+1}{2}\right)^2. \tag{B4}$$

[1] A. K. Geim and K. S. Novoselov, The rise of graphene, Nat. Mater. **6**, 183 (2007).
[2] K. Watanabe, T. Taniguchi, T. Niiyama, K. Miya, and M. Taniguchi, Far-ultraviolet plane-emission handheld device based on hexagonal boron nitride, Nat. Photonics **3**, 591 (2009).
[3] A. H. Castro Neto, F. Guinea, N. M. R. Peres, K. S. Novoselov, and A. K. Geim, The electronic properties of graphene, Rev. Mod. Phys. **81**, 109 (2009).
[4] Q. Weng, X. Wang, X. Wang, Y. Bando, and D. Golberg, Functionalized hexagonal boron nitride nanomaterials: Emerging properties and applications, Chem. Soc. Rev. **45**, 3989 (2016).
[5] K. Zhang, Y. Feng, F. Wang, Z. Yang, and J. Wang, Two dimensional hexagonal boron nitride (2D-hBN): Synthesis, properties and applications, J. Mater. Chem. C **5**, 11992 (2017).
[6] M. Ezawa, Peculiar width dependence of the electronic properties of carbon nanoribbons, Phys. Rev. B **73**, 045432 (2006).
[7] R. Murali, Y. Yang, K. Brenner, T. Beck, and J. D. Meindl, Breakdown current density of graphene nanoribbons, Appl. Phys. Lett. **94**, 243114 (2009).
[8] P. Zheng, S. E. Bryan, Y. Yang, R. Murali, A. Naeemi, and J. D. Meindl, Hydrogenation of graphene nanoribbon edges: Improvement in carrier transport, IEEE Electron Device Lett. **34**, 707 (2013).
[9] S. Das, S. Bhattacharya, D. Das, and H. Rahaman, A survey on pristine and intercalation doped graphene nanoribbon interconnect for future VLSI circuits, AIMS Mater. Sci. **8**, 247 (2021).
[10] J. M. Marmolejo-Tejada and J. Velasco-Medina, Review on graphene nanoribbon devices for logic applications, Microelectron. J. **48**, 18 (2016).
[11] V. K. Nishad, A. K. Nishad, S. Roy, B. K. Kaushik, and R. Sharma, First principle analysis of Os-passivated armchair graphene nanoribbons for nanoscale interconnects, in

Proceedings of the IEEE 20th International Conference on Nanotechnology (IEEE-NANO), Montreal, QC, Canada (IEEE, Piscataway, NJ, 2020), pp. 155–158.

[12] V. Saraswat, R. M. Jacobberger, and M. S. Arnold, Materials science challenges to graphene nanoribbon electronics, ACS Nano **15**, 3674 (2021).

[13] S. Osella, A. Narita, M. G. Schwab, Y. Hernandez, X. Feng, K. Mullen, and D. Beljonne, Graphene nanoribbons as low band gap donor materials for organic photovoltaics: Quantum chemical aided design, ACS Nano **6**, 5539 (2012).

[14] M. Mehdi Pour, A. Lashkov, A. Radocea, X. Liu, T. Sun, A. Lipatov, R. A. Korlacki, M. Shekhirev, N. R. Aluru, J. W. Lyding, V. Sysoev, and A. Sinitskii, Laterally extended atomically precise graphene nanoribbons with improved electrical conductivity for efficient gas sensing, Nat. Commun. **8**, 820 (2017).

[15] M. Fujita, K. Wakabayashi, K. Nakada, and K. Kusakabe, Peculiar localized state at zigzag graphite edge, J. Phys. Soc. Jpn. **65**, 1920 (1996).

[16] K. Nakada, M. Fujita, G. Dresselhaus, and M. S. Dresselhaus, Edge state in graphene ribbons: Nanometer size effect and edge shape dependence, Phys. Rev. B **54**, 17954 (1996).

[17] S. Behzad and R. Chegel, Thermal conductivity, heat capacity and magnetic susceptibility of graphene and boron nitride nanoribbons, Diam. Relat. Mater. **88**, 101 (2018).

[18] K. Wakabayashi, M. Fujita, H. Ajiki, and M. Sigrist, Electronic and magnetic properties of nanographite ribbons, Phys. Rev. B **59**, 8271 (1999).

[19] L. Yang, C.-H. Park, Y.-W. Son, M. L. Cohen, and S. G. Louie, Quasiparticle energies and band gaps in graphene nanoribbons, Phys. Rev. Lett. **99**, 186801 (2007).

[20] Y.-W. Son, M. L. Cohen, and S. G. Louie, Energy gaps in graphene nanoribbons, Phys. Rev. Lett. **97**, 216803 (2006).

[21] J. Nakamura, T. Nitta, and A. Natori, Electronic and magnetic properties of BNC ribbons, Phys. Rev. B **72**, 205429 (2005).

[22] C.-H. Park and S. G. Louie, Energy gaps and stark effect in boron nitride nanoribbons, Nano Lett. **8**, 2200 (2008).

[23] F.-L. Shyu, Electronic and optical properties of boron nitride nanoribbons in electric field by the tight-binding model, Phys. B: Condens. Matter **452**, 7 (2014).

[24] M. Topsakal, E. Aktürk, and S. Ciraci, First-principles study of two- and one-dimensional honeycomb structures of boron nitride, Phys. Rev. B **79**, 115442 (2009).

[25] Z. Zhang and W. Guo, Energy-gap modulation of BN ribbons by transverse electric fields: First-principles calculations, Phys. Rev. B **77**, 075403 (2008).

[26] S. Wang, Q. Chen, and J. Wang, Optical properties of boron nitride nanoribbons: Excitonic effects, Appl. Phys. Lett. **99**, 063114 (2011).

[27] J. Li, L. Z. Sun, and J. X. Zhong, Strain effects on electronic properties of boron nitride nanoribbons, Chin. Phys. Lett. **27**, 077101 (2010).

[28] Y. Ding, Y. Wang, and J. Ni, The stabilities of boron nitride nanoribbons with different hydrogen-terminated edges, Appl. Phys. Lett. **94**, 233107 (2009).

[29] V. Barone, O. Hod, and G. E. Scuseria, Electronic structure and stability of semiconducting graphene nanoribbons, Nano Lett. **6**, 2748 (2006).

[30] K. K. Jha, N. Tyagi, N. K. Jaiswal, and P. Srivastava, Structural and electronic properties of armchair graphene nanoribbons functionalized with fluorine, Phys. Lett. A **383**, 125949 (2019).

[31] S. Prabhakar and R. Melnik, *Ab-initio* calculations of strain induced relaxed shape armchair graphene nanoribbon, Phys. E **114**, 113648 (2019).

[32] H. Ren, Q. Li, H. Su, Q. W. Shi, J. Chen, and J. Yang, Edge effects on the electronic structures of chemically modified armchair graphene nanoribbons, arXiv:0711.1700.

[33] Y. Lu, R. Wu, L. Shen, M. Yang, Z.D. Sha, Y. Cai, and Y. Feng, Effects of edge passivation by hydrogen on electronic structure of armchair graphene nanoribbon and band gap engineering, Appl. Phys. Lett. **94**, 122111 (2009).

[34] H. Raza and E. C. Kan, Armchair graphene nanoribbons: Electronic structure and electric-field modulation, Phys. Rev. B **77**, 245434 (2008).

[35] B. Sarikavak-Lisesivdin, S.B. Lisesivdin, and E. Ozbay, *Ab initio* study of Ru-terminated and Ru-doped armchair graphene nanoribbons, Mol. Phys. **110**, 2295 (2012).

[36] H. Jippo and M. Ohfuchi, First-principles study of edge-modified armchair graphene nanoribbons, J. Appl. Phys. **113**, 183715 (2013).

[37] J. Dauber, B. Terrés, C. Volk, S. Trellenkamp, and C. Stampfer, Reducing disorder in graphene nanoribbons by chemical edge modification, Appl. Phys. Lett. **104**, 083105 (2014).

[38] M. G. Schwab, A. Narita, S. Osella, Y. Hu, A. Maghsoumi, A. Mavrinsky, W. Pisula, C. Castiglioni, M. Tommasini, D. Beljonne, X. Feng, and K. Müllen, Bottom-up synthesis of necklace-like graphene nanoribbons, Chem. An Asian J. **10**, 2134 (2015).

[39] T. Galvani, F. Paleari, H. P. C. Miranda, A. Molina-Sánchez, L. Wirtz, S. Latil, H. Amara, and F. Ducastelle, Excitons in boron nitride single layer, Phys. Rev. B **94**, 125303 (2016).

[40] J. P. Perdew, K. Burke, and M. Ernzerhof, Generalized gradient approximation made simple, Phys. Rev. Lett. **77**, 3865 (1996).

[41] P. Giannozzi, S. Baroni, N. Bonini, M. Calandra, R. Car, C. Cavazzoni, D. Ceresoli, G. L. Chiarotti, M. Cococcioni, I. Dabo *et al.*, QUANTUM ESPRESSO: A modular and open-source software project for quantum simulations of materials, J. Phys.: Condens. Matter **21**, 395502 (2009).

[42] D. R. Hamann, Optimized norm-conserving Vanderbilt pseudopotentials, Phys. Rev. B **88**, 085117 (2013).

[43] M. Posternak, A. Baldereschi, A. J. Freeman, E. Wimmer, and M. Weinert, Prediction of electronic interlayer states in graphite and reinterpretation of alkali bands in graphite intercalation compounds, Phys. Rev. Lett. **50**, 761 (1983).

[44] M. Posternak, A. Baldereschi, A. J. Freeman, and E. Wimmer, Prediction of electronic surface states in layered materials: Graphite, Phys. Rev. Lett. **52**, 863 (1984).

[45] X. Blase, A. Rubio, S. G. Louie, and M. L. Cohen, Quasiparticle band structure of bulk hexagonal boron nitride and related systems, Phys. Rev. B **51**, 6868 (1995).

[46] F. Paleari, First-Principles Approaches to the Description of Indirect Absorption and Luminescence Spectroscopy: Exciton-Phonon Coupling in Hexagonal Boron Nitride, Ph.D. thesis, University of Luxembourg, 2019.

[47] S. Latil, H. Amara, and L. Sponza, Structural classification of boron nitride twisted bilayers and ab initio investigation of their stacking-dependent electronic structure, SciPost Phys. **14**, 053 (2023).

[48] X. Blase, L. X. Benedict, E. L. Shirley, and S. G. Louie, Hybridization effects and metallicity in small radius carbon nanotubes, Phys. Rev. Lett. **72**, 1878 (1994).

[49] X. Blase, A. Rubio, S. G. Louie, and M. L. Cohen, Stability and band gap constancy of boron nitride nanotubes, Europhys. Lett. **28**, 335 (1994).

[50] S. Hu, J. Zhao, Y. Jin, J. Yang, H. Petek, and J. G. Hou, Nearly free electron superatom states of carbon and boron nitride nanotubes, Nano Lett. **10**, 4830 (2010).